Impacts of Uncertain Geomagnetic Disturbances on Transient Power Angle Stability of DFIG Integrated Power System

Si, Yuan; Wang, Zezhong ; Liu, Lianguang ; Anvari-Moghaddam, Amjad

Published in:
I E E E Transactions on Industry Applications

DOI (link to publication from Publisher):
10.1109/TIA.2022.3231582

Publication date:
2023

Document Version
Accepted author manuscript, peer reviewed version

Impacts of Uncertain Geomagnetic Disturbances on Transient Power Angle Stability of DFIG Integrated Power System

Yuan Si
North China Electric Power University
Beijing, China
Beinong road No.2
Beijing, 10206 China
siy@ncepu.edu.cn

Zezhong Wang
North China Electric Power University
Beijing, China
Beinong road No.2
Beijing, 10206 China
wzzh@ncepu.edu.cn

Lianguang Liu
North China Electric Power University
Beijing, China
Beinong road No.2
Beijing, 10206 China
liulianguang@ncepu.edu.cn

Amjad Anvari-Moghaddam
Senior Member, IEEE
Aalborg University
9220 Aalborg, Denmark
aam@energy.aau.dk

***Abstract* -- When geomagnetic disturbances (GMDs) occur, the reactive power loss (GIC-Q) caused by geomagnetically induced currents (GICs) flowing through transformers can lead to system instability. Previous studies have been focused on the impacts of GMD on the static stability of conventional systems, while transient stability of hybrid systems left unexplored. In this paper a hybrid system based on wind and conventional energy sources are proposed as a research object. The wind farm output power and GIC-Q are equivalent to the grounding impedance. Considering the uncertainty of GMD, based on establishing the random fuzzy model of induced geomagnetic fields, the expected value of critical clearing angle and acceleration/deceleration area is calculated by using credibility theory. Then the influence of GMD on the transient stability under the different proportions of wind farm output power is analyzed quantitatively by using transient stability margin. Taking the Mengdong power grid under four operation modes as an example, the results show that no matter which operation mode, the transient stability of the system is reduced when GMDs occur. Under heavy loading conditions in summer and when the proportion of wind farm output power reaches 50%, the transient stability of the system is the lowest. The research results provide a basis for disaster prevention and control of GMDs.**

***Index Terms*--Hybrid system, induced geomagnetic fields, geomagnetic disturbances, GIC-Q, transient stability.**

I. INTRODUCTION

The quasi-dc geomagnetically induced current (GICs) flowing through transformers can generate reactive loss (GIC-Q) [1,2]. Due to the large number of transformers in the power system and the uncertainty of geomagnetic disturbances (GMDs) intensity, it may threaten the stability of the system when it is added to the system as reactive loads [3]. At present, the research is directed toward analyzing the impact of GMDs on conventional power systems and the efforts are mainly limited to static voltage stability. With the development of wind power, the proportion of wind power in power grids is increasing. Whether GMDs will affect the transient stability of hybrid systems remains to be studied.

During the geomagnetic storm on March 12-13, 1989, the Quebec power grid suffered an 8 V/km of induced geomagnetical field (IGF), resulting in a severe blackout and huge economic losses [4]. During the geomagnetic storm on May 10, 1992, the monitoring data of 345 kV/115 kV transformer in a substation by EPRI company of the United States showed that the Q_{GIC} was very large [5]. Even though GMD events are rare in comparison with other more common uncertain events, it has been identified as a "high-impact, low-frequency" extreme event causing risk to the power system as stated in the report from the U.S. Department of Energy [6]. The North American Electric Reliability Corporation (NERC) in February 2012 special reliability assessment report on GMDs notes that there are potential for damage to high voltage transformers and system stability operation [7]. South Africa [8], New Zealand [9], Australia and other countries in the mid-low-latitude also put forward the risk of GMD disaster faced by the power system [10].

Concerning the induced geoelectric field data in the analysis of the impact of GMDs on system stability, references [11] and [12] respectively use the amplitude of IGF in a geomagnetic storm event or the assumed value of 1V/km to study the impact of GMDs on voltage stability. However, in reality, the amplitude and direction of the IGF usually keeps changing. Because IGFs with different amplitudes and directions can introduce significantly different GIC-Q into the same system, the impact of GMDs can be very different. The assumption of a constant IGF significantly limits the practicality of previous studies. Considering that there are a large number of transformers in the system, it is impossible to statistically analyze the GIC-Q of each transformer, so the root cause (induced geoelectric field) is analyzed by using multiple GMDs in the 23rd solar activity cycle [13]. It is found that the probability distribution model of induced geoelectric field is lognormal distribution. However, the parameters of probability density function

(PDF) are not a certain value, and it is difficult to obtain clear probability parameters of PDF parameters due to the limitation of GMDs data. Therefore, the parameters of the induced geoelectric field PDF in multiple GMDs are fuzzy. On the one hand, if the Montero sampling method is used to sample each GMD induced geoelectric field, the calculation cost is too high. On the other hand, using random variables to describe the induced geoelectric field itself does not accord with the objective reality. Given the uncertainty of GMDs, it is necessary to propose an induced geoelectric field model that can comprehensively describe its randomness and fuzziness to study the influence of GMDs on system stability.

The GIC-Q is the main reason threatening the stable operation of the system. Authors of [14] analyzed the impact and consequences of GMDs on power systems from two aspects of power transformer half-wave saturation and voltage instability. The amplitude of GIC was taken as an index in [15] and divided the risk of power grid geomagnetic storm into "low", "medium", "high" and "extreme". Reference [16] proposed the theoretical framework of power grid security risk assessment under the influence of GMDs and the concept of GMDs-electrical hybrid simulation. These research works were mainly based on conventional systems neglecting the contribution of renewables (such as wind power) in dynamic system behavior Whether different wind power output proportions can affect the anti-GMD ability of the system has not been studied yet. In addition, the impact of GMDs on power system stability has primarily been focused on the size of GIC or the risk of voltage instability caused by GIC-Q [17]. More importantly, the change of GIC-Q caused by the change of network topology during normal operation, failure and after fault removal has not been considered so far. Whether it can affect the transient stability of the system and how to quantitatively evaluate this impact remain to be further studied.

Taking the 29 strong geomagnetic storms in the 23rd solar cycle as typical cases [18], the t location-scale PDF is used to fit the induced geoelectric field components. Considering that the PDF of induced geoelectric fields can be determined and the distribution parameters are fuzzy, a random fuzzy model of induced geoelectric field is proposed. The equivalent grounding impedance is used to replace GIC-Q and wind farm output power, and their influence on the electromagnetic power of synchronous generators is transformed into the influence on the electrical connection between synchronous generators, then the GMDs is connected with the inertia, mechanical power and electromagnetic power in the equivalent rotor motion equation. Through fuzzy simulation calculation, the influence of GMDs on the transient power angle stability of hybrid systems with different levels of wind power output power is quantitatively analyzed under various operation modes, which provides a basis for the treatment of geomagnetic storm disasters. The contributions of this paper are as follows:

- Based on several GMDs events, a stochastic fuzzy model of IGF is established.
- Based on the stochastic fuzzy model of IGF and credibility theory, a model to quantify the influence of GMDs on transient power angle stability is proposed.
- Taking the doubly fed induction generator (DFIG) as an example, the influence of wind power on the anti-GMDs ability of the system is studied.

II. Analysis of Random Fuzziness of Induced Geoelectric Fields

A. Probability distribution characteristics of induced geoelectric fields

The layered earth resistivity model is established by using the earth conductivity data in the Mengdong area [12], as shown in Fig. 1, where ρ and h represent the resistivity and thickness of each layer respectively.

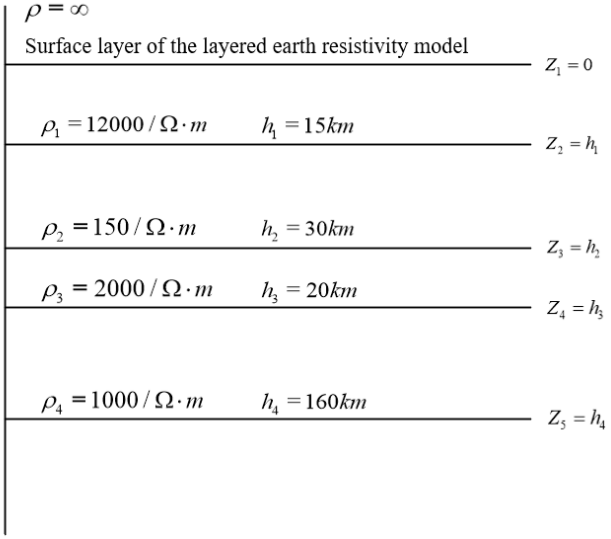

Fig. 1. Layered model of earth resistivity in Mengdong.

Taking the geomagnetic field data recorded by Beijing Geomagnetic Station for 29 strong geomagnetic storms in the 23rd solar cycle as an example [13,18], the IGF is calculated by combining layered model of earth resistivity and plane wave method [19, 20]. The uncertainty of GMD intensity makes induced geomagnetic fields fluctuate. Determining the PDF of induced geomagnetic fields is the basis for studying the impact of multiple GMDs on system stability. To quantitatively compare the fitting effect of each PDF, a fitting index is defined, as shown in (1).

$$I = \sum_{i=1}^{M} (y_i - \overline{N_i}) \tag{1}$$

where M is the number of groups of frequency distribution histogram; $y_i = f\left(\overline{C_i}\right)$, $\overline{N_i}$ and $\overline{C_i}$ are the height and center position of the *i*-th straight square column respectively; $f(\cdot)$ is the fitted PDF; y_i is the value corresponding to the fitting probability density function at the center position $\overline{C_i}$. The smaller the fitting index *I*, the higher the fitting accuracy.

Using different distribution functions to fit the induced geoelectric field components of 29 GMD events, the fitting

index values are obtained. The average, maximum and minimum values are shown in Table I.

TABLE I
INDUCED GEOELECTRIC FIELD FITTING INDEX VALUE

Induced geoelectric fields	Index	Type of disturbance		
		Normal	t location - scale	Cauchy
E_x	Max	0.893	0.225	0.379
	Min	0.802	0.107	0.203
	Ave	0.851	0.116	0.318
E_y	Max	0.658	0.336	0.671
	Min	0.421	0.159	0.502
	Ave	0.556	0.211	0.591

It can be seen from Table I that t location-scale distribution has the best fitting effect on the East-West component E_x and North-South component E_y. The PDF of induced geoelectric field components is obtained by fitting the t location-scale distribution function shown in (2), as shown in Fig. 2.

$$f(x)=\frac{\Gamma\left(\frac{\upsilon+1}{2}\right)}{\sigma\sqrt{\upsilon\pi}\Gamma\left(\frac{\upsilon}{2}\right)}\left[\frac{\upsilon+\left(\frac{x-\mu}{\sigma}\right)^2}{\upsilon}\right]^{-\frac{\upsilon+1}{2}} \tag{2}$$

where $\Gamma(\cdot)$ is the gamma function. μ is the position parameter. σ is the scale parameter. υ is the shape parameter.

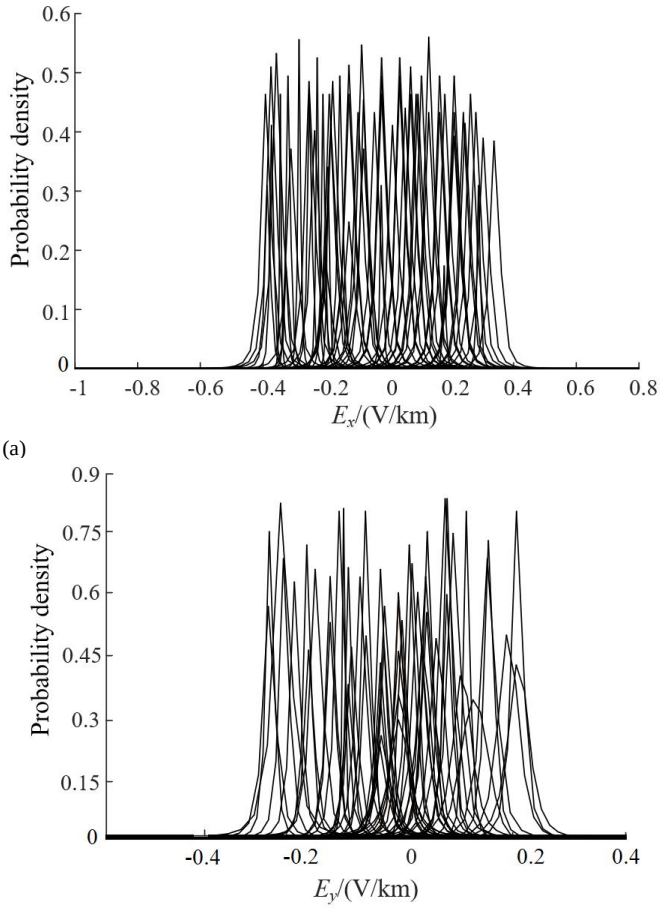

Fig. 2. Fitting of induced geoelectric fields of 29 GMDs: (a) E_x probability density distribution. (b) E_y probability density distribution.

Due to the uncertainty of induced geoelectric fields, its PDF is not a single curve, but cluster of PDF curves with different distribution parameters.

B. Fuzzy uncertainty analysis of probability distribution parameters of induced geoelectric field

The parameters of the induced geoelectric field PDF of 29 geomagnetic storm events are counted by frequency according to the interval, and the frequency distribution diagram of the parameters is obtained, as shown in Fig. 3.

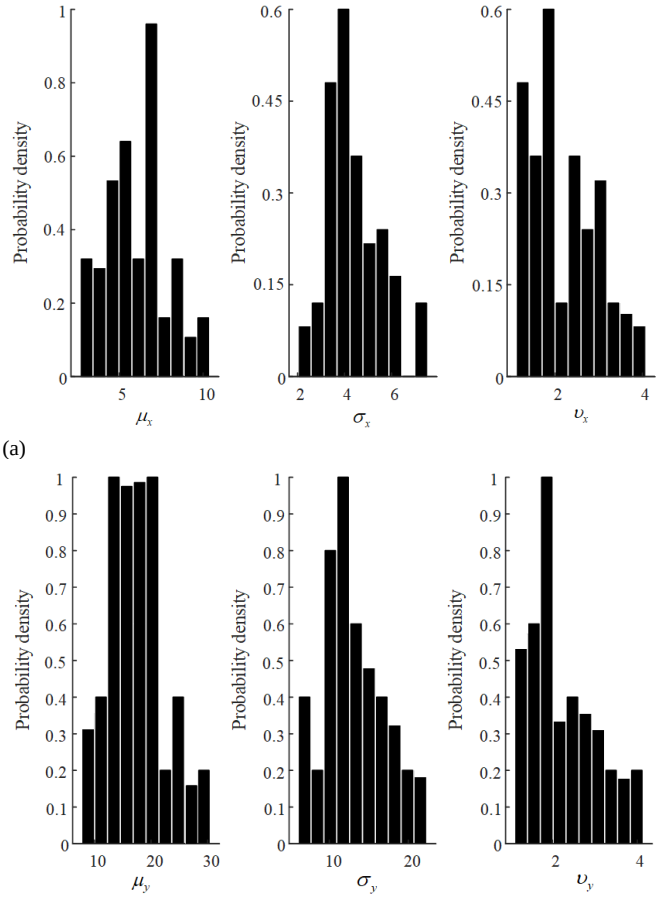

Fig. 3. PDF parameter distribution of induced geoelectric fields: (a) PDF parameter frequency distribution of E_x. (b) PDF parameter frequency distribution of E_y.

For the PDF parameter of E_x, the value of μ_x is approximately centered on 6.911. With the gradual increase of the distance from the center, the occurrence frequency of its value shows a downward trend except for the parameter values of some special points. If considering excluding the influence of special parameter values, μ_x can be approximately described by triangular fuzzy variables. The values of σ_x and υ_x are approximately centered on 3.957 and 1.845 respectively. They show an attenuation trend with the gradual increase of the distance from the center, which can also be described by triangular fuzzy variables. Considering a 95% confidence level, the confidence intervals

of μ_x, σ_x and υ_x of E_x are [3.042, 10.01], [2.304, 7.263] and [1.25, 3.929], respectively. For the PDF parameter of E_y, the value of μ_y is approximately centered on 16.911. In a certain area [13.44, 20.26] around the value, the occurrence frequency of parameter values is relatively concentrated, and the occurrence frequency of values outside the area shows an attenuation trend. It is more appropriate to use a trapezoidal fuzzy variable to describe it. The σ_y and υ_y are approximately centered on 11.76 and 1.866 respectively and are described by triangular fuzzy variables. At the 95% confidence level, the confidence intervals of E_y's μ_x, σ_x and υ_x are [8.902, 29.34], [6.869, 21.53], and [1.26, 3.989], respectively. The membership functions of PDF parameters of E_x are shown in (3) ~ (5), and the membership functions of PDF parameters of E_y are shown in (6) ~ (8).

$$f(\mu_x)=\begin{cases}0.258\mu_x-0.786, & 3.042\le\mu_x\le 6.911\\ -0.322\mu_x+3.23, & 6.911<\mu_x\le 11.1\\ 0, & \mu_x<3.042 \text{ or } \mu_x>11.1\end{cases} \tag{3}$$

$$f(\sigma_x)=\begin{cases}0.604\sigma_x-1.393, & 2.304\le\sigma_x\le 3.957\\ -0.302\sigma_x+2.167, & 3.957<\sigma_x\le 7.263\\ 0, & \sigma_x<2.304 \text{ or } \sigma_x>7.263\end{cases} \tag{4}$$

$$f(\upsilon_x)=\begin{cases}1.681\upsilon_x-2.101, & 1.25\le\upsilon_x\le 1.845\\ -0.479\upsilon_x+1.885, & 1.845<\upsilon_x\le 3.929\\ 0, & \upsilon_x<1.25 \text{ or } \upsilon_x>3.929\end{cases} \tag{5}$$

$$f(\mu_y)=\begin{cases}(\mu_y-8.902)/4.538, & 8.902\le\mu_y<13.44\\ 1, & 13.44\le\mu_y<20.26\\ (29.34-\mu_y)/9.08, & 20.26\le\mu_y<29.34\\ 0, & \mu_y<8.902 \text{ or } \mu_y>29.34\end{cases} \tag{6}$$

$$f(\sigma_y)=\begin{cases}0.204\sigma_y-1.404, & 6.869\le\sigma_y\le 11.76\\ -0.102\sigma_y+2.204, & 11.76<\sigma_y\le 21.53\\ 0, & \sigma_y<6.869 \text{ or } \sigma_y>21.53\end{cases} \tag{7}$$

$$f(\upsilon_y)=\begin{cases}1.65\upsilon_y-2.079, & 1.26\le\upsilon_y\le 1.866\\ -0.471\upsilon_y+1.879, & 1.866<\upsilon_y\le 3.989\\ 0, & \upsilon_y<1.26 \text{ or } \upsilon_y>3.989\end{cases} \tag{8}$$

In statistical problems, when the distribution of a random variable is known and its parameter value is described as a fuzzy variable, the random variable will become a random fuzzy variable [21,22]. The induced geoelectric field component satisfies this characteristic, so it is defined as a random fuzzy variable to study its influence on the transient power angle stability.

The random fuzzy variables ξ_{E_x} and ξ_{E_y} are used to represent E_x and E_y, and the chance measure distribution function of t location-scale distribution is shown in (9).

$$F_{x/y}\left(\xi_{E_{x/y}}\right)=Ch(E_{x/y}<\xi_{E_{x/y}}) \tag{9}$$

where $F(\cdot)$ is cumulative probability density (CDF) function. $Ch(\cdot)$ is chance measure operator.

C. Random fuzzy simulation method of induced geoelectric fields

Random fuzzy simulation technology and inverse transformation method are used to generate induced geoelectric field samples [23]. The specific steps are as follows:

1) Based on the chance measure distribution function of induced geoelectric field, *M* distributed parameter samples of $P_{os}\{\cdot\}\ge\varepsilon$ are extracted from the confidence intervals of parameters $\mu_{x/y}$, $\sigma_{x/y}$, and $\upsilon_{x/y}$, where P_{os} is the possibility measure and ε is a sufficiently small positive number.

2) The extracted *M* μ_{xi}, σ_{xi}, υ_{xi} are matched into corresponding combinations, and the values of $P_{os}\{\mu_{xi},\sigma_{xi},\upsilon_{xi}\}$ are generated by simulation in the interval [0,1].

3) The parameter combination obtained in step 2) is taken as the t location-scale parameter, and the inverse function of (9) is solved to obtain the value $\xi_{E_{xi/yi}}=F_x^{-1}\left[Ch(E_{x/y}<\xi_{E_{xi/yi}})\big|_{(\mu_{xi/yi},\sigma_{xi/yi},\upsilon_{xi/yi})}\right]$ of the induced geoelectric field. The possibility of the occurrence of the geoelectric field component is the possibility measure $P_{os}\{\mu_{xi},\sigma_{xi},\upsilon_{xi}\}$ of the combination of $\{\mu_{xi},\sigma_{xi},\upsilon_{xi}\}$, denoted by $v_{xk}=P_{os}\{\mu_{xi},\sigma_{xi},\upsilon_{xi}\}$, $v_{yk}=P_{os}\{\mu_{yi},\sigma_{yi},\upsilon_{yi}\}$.

4) The induced geoelectric field components $\xi_{E_{xi}}$ and $\xi_{E_{yi}}$ are randomly combined into induced geoelectric field $\left(\xi_{E_{xi}},\xi_{E_{yi}}\right)$, and its possibility measure v_k is $v_{xk}\cdot v_{yk}$.

In practical operation, since the specific expression of the inverse function cannot be given directly, the graphical method is used for calculation, that is, the CDF curve is obtained by using the parameter sample $\{\mu_{xi},\sigma_{xi},\upsilon_{xi}\}$, the horizontal axis is the size of E_x, the vertical axis is the probability density. The point $P_{os}\{\mu_{xi},\sigma_{xi},\upsilon_{xi}\}$ on the vertical axis is known, and the corresponding $\xi_{E_{xi}}$ is found. The acquisition method of $\xi_{E_{yi}}$ is the same.

III. IMPACT OF GMDS ON TRANSIENT STABILITY

A. Equivalent model of wind farm output power and GIC-Q

According to the extended equal area criterion (EEAC), when the multi-machine system is disturbed, the generators are divided into two clusters, the heavily disturbed cluster (S-group) and the remaining cluster (R-group) based on the degree of disturbance. According to the characteristics of generators which are in the heavily disturbed cluster, they can be equivalent to an equivalent generator *S*. Similarly, the remaining cluster is equivalent to an equivalent generator *R*. The extended dual-machine system is shown in Fig. 4. All nodes in the system are divided into four categories: potential

node in S-group (node 1) and potential node in R-group (node 2), wind farm access node W (node 3) and power exchange node L in the network (nodes 4, 5, 6 and 7).

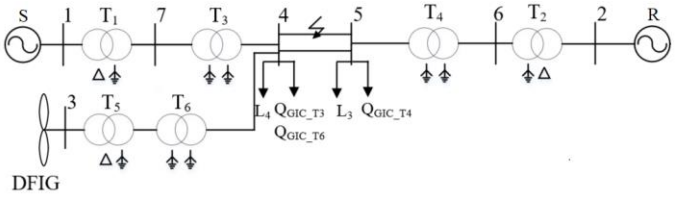

Fig. 4. Wiring diagram of extended dual-machine system

In the case of GMDs, the potential difference occurs at the grounding points of transformers in different geographical locations, which forms a loop through the ground and transmission lines to generate GIC. Half-wave saturation occurs when quasi-DC current GIC flows through the transformer, and the reactive power loss of the transformer increases. This part of reactive power loss is added to the system as a reactive load. The flow path of GIC is shown in Fig. 5.

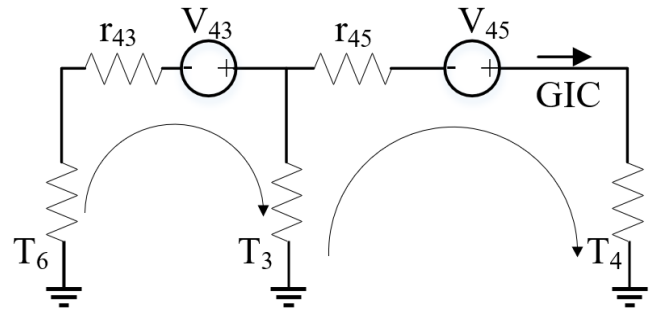

(a)

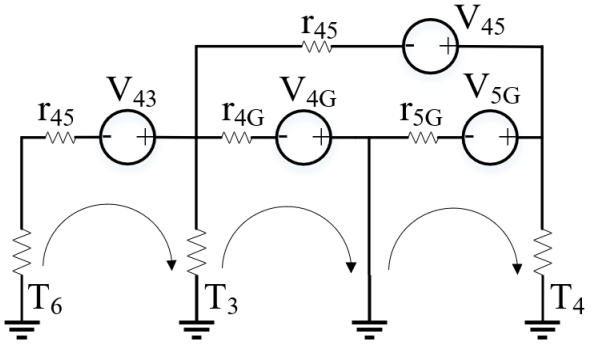

(b)

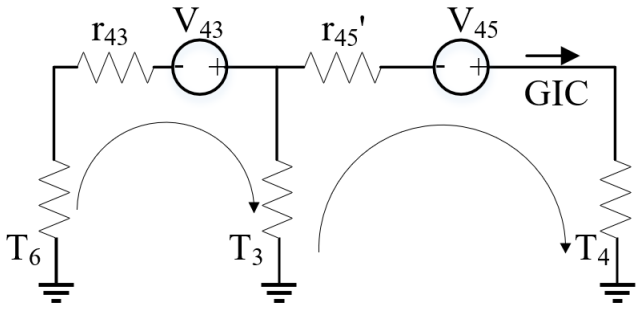

(c)

Fig. 5. GIC circulation path: (a) GIC flow path during normal operation. (b) GIC flow path in short circuit fault. (c) GIC flow path after fault removal.

Whether it is normal operation, short-circuit fault or after clearing fault, GIC-Q can be used as a reactive load, but its size will change with the change of GMD intensity and network topology. The impedance model is used to represent the reactive load like GIC-Q. Therefore, GIC-Q can be equivalent to a positive reactance under normal conditions, short-circuit fault and fault removal, as shown in (10).

$$X_{Q_{GICi}} = j\frac{Q_{GICi}}{U_{Q_{GICi}}^2} \tag{10}$$

where, $X_{Q_{GICi}}$ is the reactance. $U_{Q_{GICi}}$ is the node voltage of the transformer node generating GIC-Q. Q_{GICi} is the reactive power loss caused by GIC flowing through the transformer, which is calculated by k-value method [24,25]. $i=1,2,3$ respectively represent normal, faulty, and fault removal conditions.

Assuming that the wind farm access node W is inside the S -group and generators in wind farms are doubly-fed asynchronous generators (DFIGs) when the wind power access ratio is k_S, the active power output of the wind farm is $P_W = k_S P_{m.S0}$ and $P_{m.S0}$ is the mechanical power of the S-group.

Under normal conditions, DFIG only provides active power to the system, which can be equivalent to a negative resistance R_{W1}. In the case of fault, DFIG terminal voltage drops. To recover the terminal voltage, DFIG with low voltage ride through capability sends reactive power to the system under the action of the control system. Therefore, the wind farm output power is equivalent to a parallel negative resistance R_{W2} and negative reactance X_{W1}. After fault removal, DFIG not only generates active power, but also emits a small amount of reactive power. Therefore, the wind farm output power is equivalent to a negative impedance with negative resistance R_{W3} and negative reactance X_{W3} in parallel. The equivalent impedance is shown in (11) and (12).

$$R_{Wi} = \frac{U_{Wi}^2}{P_{Wi}} (i=1,2,3) \tag{11}$$

$$X_{Wi} = \frac{U_{Wi}^2}{Q_{Wi}} (i=1,2) \tag{12}$$

where, U_{W1} is the voltage of DFIG access nodes. P_{Wi} and Q_{Wi} are the active power and reactive power of DFIG. $i=1,2,3$ respectively represent three states: normal, fault and fault removal.

According to the power characteristics of generators in a multi-machine power system, the electromagnetic power output by any generator in the system is a function of the internal potential, power angle and network parameters of all generators. To analyze the transient stability of the multi-synchronous power system, the node voltage equation of the system should be equivalently transformed, and the nodes

expect nodes 1 and 2 should be contracted. According to the node classification and by eliminating nodes 3, 6 and 7, the node voltage equation of the system can be derived as (13).

$$\begin{pmatrix} Y_{11i} & Y_{12i} & Y_{14i} & Y_{15i} \\ Y_{21i} & Y_{22i} & Y_{24i} & Y_{25i} \\ Y_{41i} & Y_{42i} & Y_{44i\_0} & Y_{45i} \\ Y_{51i} & Y_{52i} & Y_{54i} & Y_{55i\_0} \end{pmatrix} \begin{pmatrix} \boldsymbol{E}_{1i} \\ \boldsymbol{E}_{2i} \\ \boldsymbol{U}_{4i} \\ \boldsymbol{U}_{5i} \end{pmatrix} = \begin{pmatrix} \boldsymbol{I}_{1i} \\ \boldsymbol{I}_{2i} \\ 0 \\ 0 \end{pmatrix} \tag{13}$$

where Y_{44i_0} and Y_{55i_0} are the self-admittance of nodes 4 and 5 without GMD and wind farm respectively.

When GMDs occur and wind farm power output changes, Y_{44i_0} is corrected to Y_{44i}, $Y_{44i} = Y_{44i\_0} + 1/Z_{Wi} + 1/X_{Q_{GICi}}$. Y_{55i_0} is corrected to Y_{55i}, $Y_{55i} = Y_{55i\_0} + 1/X_{Q_{GICi}}$. Nodes 4 and 5 are further eliminated, as shown in (14).

$$\begin{pmatrix} Y_{11} - Y(k_S, Q_{GIC}) & Y_{12} - Y(k_S, Q_{GIC}) \\ Y_{21} - Y(k_S, Q_{GIC}) & Y_{22} - Y(k_S, Q_{GIC}) \end{pmatrix} \begin{pmatrix} \boldsymbol{E}_1 \\ \boldsymbol{E}_2 \end{pmatrix} = \begin{pmatrix} \boldsymbol{I}_1 \\ \boldsymbol{I}_2 \end{pmatrix} \tag{14}$$

where $Y(k_S, Q_{GIC})$ is the correction of admittance. Because the expression is complex, it is expressed in function form.

Nodes 4 and 5 are not simply removed, but the information of GMDs and wind farm output power is integrated into the node admittance matrix of synchronous generator, that is, the influence of GMD and wind farm output power on the electromagnetic power of synchronous generators is transformed into the influence on the electrical connection between synchronous generators.

B. Influence of GMDs on equivalent rotor motion equation of hybrid system

When the proportion of wind farm output power changes, the system changes the total output power by changing the number of synchronous generators, so as to maintain the power balance of the system. Assuming there is no wind farm, the number of synchronous generators of *S* is *N*, the inertia time coefficient M_{S0} and total mechanical power $P_{m.S0}$ of *S* are shown in (15).

$$\begin{cases} M_{S0} = \sum_{i=1}^{N} M_i \\ P_{m.S0} = \sum_{i=1}^{N} P_{m.i} \end{cases} \quad i \in S \tag{15}$$

where, M_i and M_j ($i \in S$, $j \in R$) are inertia time coefficients of generators. M_S and M_R are inertia time coefficients of S-group and R-group. $P_{m.i}$ and $P_{m.j}$ ($i \in S$, $j \in R$) are mechanical power of generators. $P_{m.S}$ and $P_{m.R}$ are mechanical power of S-group and R-group.

When the proportion of wind farm output power is k_S, the output power of conventional generators is (1- k_S) $P_{m.S0}$, and the number of synchronous generator is (1- k_S)*N* at this time is (1-k_S) *N*. Combining with (15), the $M_S(k_S)$ and $P_{m.S}(k_S)$ are shown in (16) [26].

$$\begin{cases} M_S(k_S) = \sum_{i=1}^{(1-k_S)N} M_i = (1-k_S) M_{S0} \\ P_{m.S}(k_S) = \sum_{i=1}^{(1-k_S)N} P_{m.i} = (1-k_S) P_{m.S0} \end{cases} \quad i \in S \tag{16}$$

where M_{S0} is the equivalent inertia time coefficient of S-group without wind power access. $P_{m.S0}$ is the equivalent mechanical power of S-group without wind power.

The rotor motion equations of equivalent synchronizers *S* and *R* are subtracted, and the extended two-machine system is equivalent to a single machine infinite bus system. By analyzing the influence of GMD and wind power access ratio on the mechanical power and electromagnetic power, the influence is reflected in the variation relationship between each parameter in the equivalent rotor motion equation and k_S, Q_{GIC}, as shown in (17).

$$\begin{aligned} M_{SR}(k_S)\ddot{\delta}_{SR} &= P_{m.SR}(k_S) - P_{e.SR}(k_S, Q_{GIC}) \\ &= P_{m.SR}(k_S) - \left[P_C(k_S) - \Delta P_{eS}(k_S, Q_{GIC}) - \right. \\ &\left. \Delta P_{eR}(k_S, Q_{GIC}) + P_{\max}(k_S, Q_{GIC}) \sin\left[\delta_{SR} + \gamma(k_S, Q_{GIC})\right]\right] \end{aligned} \tag{17}$$

where, M_{SR} is the equivalent inertial time coefficient. $P_{m.SR}$ and $P_{e.SR}$ are equivalent mechanical power and electromagnetic power respectively. Because the expression of parameters is complex, they are expressed in the form of k_S and Q_{GIC} functions.

$$M_{SR} = \frac{(1-k_S) M_{S0} M_R}{(1-k_S) M_{S0} + M_R} \tag{17-1}$$

$$\begin{aligned} P_C(k_S, Q_{GIC}) &= \frac{M_R \sum_{i\in S}\sum_{k\in S} E_i E_k G_{ik}(k_S, Q_{GIC})}{(1-k_S) M_{S0} + M_R} \\ &- \frac{(1-k_S) \sum_{j\in R}\sum_{k\in R} E_j E_l G_{jl}(k_S, Q_{GIC})}{(1-k_S) M_{S0} + M_R} \end{aligned} \tag{17-2}$$

$$\Delta P_{eS}(k_S, Q_{GIC}) = \frac{\sum_{i\in S}\sum_{k\in S} E_i E_k \Delta G_{ik}(k_R, Q_{GIC})}{(1-k_S) M_{S0} + M_R} \tag{17-3}$$

$$\Delta P_{eR}(k_S, Q_{GIC}) = \frac{(1-k_S) \sum_{j\in R}\sum_{l\in R} E_j E_l \Delta G_{jl}(k_R, Q_{GIC})}{(1-k_S) M_{S0} + M_R} \tag{17-4}$$

$$P_{\max}(k_S, Q_{GIC}) = \frac{\sqrt{C^2 + D^2} \sin\left[\delta_{SR} - \gamma\right]}{M_{SR}} \tag{17-5}$$

$$C(k_S, Q_{GIC}) = \frac{M_R - (1-k_R) M_{S0}}{(1-k_S) M_{S0} + M_R} \sum_{i\in S}\sum_{j\in R} E_i E_j G_{ij}(k_S, Q_{GIC}) \tag{17-6}$$

$$D(k_S, Q_{GIC}) = \sum_{i\in S}\sum_{j\in R} E_i E_j B_{ij}(k_S, Q_{GIC}) \tag{17-7}$$

$$\gamma(k_S, Q_{GIC}) = -\arctan\frac{C}{D} \tag{17-8}$$

It can be seen from (17) that the equivalent mechanical power and electromagnetic power of the system will be affected by k_S and GIC-Q. Therefore, the influence of GMDs on the transient stability of hybrid systems is transferred to

the influence of k_S and GIC-Q on the acceleration/deceleration area formed by the rotor motion equation.

C. Evaluation of influence of GMDs on transient stability of hybrid system

Using the induced geoelectric field samples obtained in section II-C, the expected value information of parameters related to system transient stability under the influence of GMD is calculated. The specific steps are as follows:

1) Combined with the power grid structure parameters and k-value method, the *M*-group sampling value $\left(\xi_{E_{xi}}, \xi_{E_{yi}}\right)$ is calculated which ultimately help to obtain the *M*-group GIC-Q sample of the substation.

2) Determine a certain wind power access proportion k_S, and calculate the critical clearing angle samples δ_c, acceleration area S_{ac} and deceleration area S_{dc} in combination with *M*-group GIC-Q. The minimum critical clearing angle, the minimum acceleration area and the minimum deceleration area are recorded as δ_{cmin}, S_{acmin} and S_{dcmin}. The maximum critical clearing angle, the maximum acceleration area and the maximum deceleration area are recorded as δ_{cmax}, S_{acmax} and S_{dcmax}.

3) Carry on *M* cycle, and r_δ, r_{ac} and r_{dc} are randomly generated from $[\delta_{cmin}, \delta_{cmax}]$, $[S_{acmin}, S_{acmax}]$ and $[S_{dcmin}, S_{dcmax}]$, respectively. Let e_δ=0, e_{ac}=0, e_{dc}=0.

4) Accumulate e_δ and $e_{S_{ac/dc}}$ in each cycle according to (18) and (19).

$$e_\delta = e_\delta + \frac{1}{2}\left(\max_{1\le k\le M}\{v_k \mid \delta_\delta \ge r_\delta\} + \min_{1\le k\le M}\{1-v_k \mid \delta_\delta < r_\delta\}\right) \quad (18)$$

$$e_{S_{ac/dc}} = e_{S_{ac/dc}} + \frac{1}{2}\left(\max_{1\le k\le M}\{v_k \mid S_{ac/dc} \ge r_{ac/dc}\} + \min_{1\le k\le M}\{1-v_k \mid S_{ac/dc} < r_{ac/dc}\}\right) \quad (19)$$

5) Calculate the expected value of the critical clearing angle $E[\delta_c] = \delta_{c\min} + e_\delta \times (\delta_{c\max} - \delta_{c\min})/M$. Calculate the expected value of acceleration/deceleration area $E[S_{ac/dc}] = S_{ac\min/dc\min} + e_{ac/dc} \times (S_{ac\max/dc\max} - S_{ac\min/dc\min})/M$.

The difference between deceleration area and acceleration area divided by acceleration area is defined as transient stability margin, as shown in (20).

$$\eta = \frac{S_{de} - S_{ac}}{S_{ac}} \times 100\% \quad (20)$$

where, S_{ac} and S_{de} are the expected values of acceleration area and deceleration area respectively. η is the transient stability margin.

IV. Example Analysis

A. GIC-Q under normal operation and fault conditions

The structure of the Mengdong power grid and GIC calculation results are shown in Fig. 6, where the size of the dot indicates the size of the substation GIC, the thickness of the line indicates the size of the line GIC, the color of the circle indicates the flow direction of the substation GIC, the red substation names indicate the 500 kV network, and the black is 220 kV network. It is assumed that a three-phase short-circuit fault occurs at the midpoint of branch XL-LD at t =1s, and the fault is removed at 1.3 s. According to the identification method of coherent generator group in [27], the division result of coherent generator group is obtained.

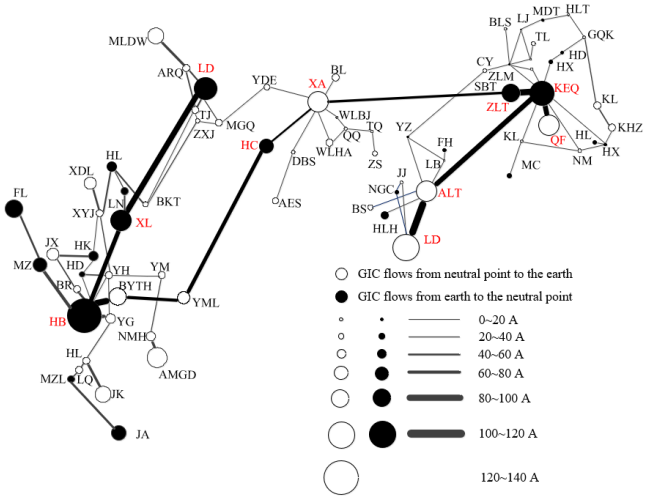

Fig. 6. GIC level of the Mengdong power grid

Since the data collected from geomagnetic stations are GMD second data and the fault duration is short, it is considered that the GMDs intensity remains unchanged during the fault. Taking E_x = 0.8 V/km, E_y = 0.4 V/km as an example, the GIC-Q of the nine 500kV substations during normal operation, fault and fault removal are shown in Table II. The difference outside the brackets are the changing rate when the fault occurs compared to the normal operation. The difference inside the brackets are the changing rate when the fault is removed compared to the normal operation.

TABLE II
GIC-Q OF EACH SUBSTATION BEFORE AND AFTER FAULT

Substation	GIC-Q/MVar			Difference/%
	Normal operation	Fault	Fault removal	
HB	356.7	178.9	205.6	49.8(42.4)
BY	347.6	134.6	205.3	61.3(40.9)
XL	178.1	131.2	106.9	26.3(39.9)
LD	532.9	226.8	367.3	57.4(31.1)
XA	232.4	118.9	200.8	48.8(13.6)
KEQ	465.3	247.1	301.0	46.9(35.3)
QF	615.4	386.3	469.2	37.2(23.8)
ALT	239.5	114.3	101.8	52.2(57.5)
LD	485.1	352.3	298.3	27.4(38.5)

By comparing the GIC-Q of each substation in three cases of normal, faulty and fault removal conditions in Table II, it can be seen that the change of network topology can change the flow path of GIC, and then affect the value of GIC-Q. Therefore, the GIC-Q of each substation in three cases and the corresponding node voltage are used to calculate the equivalent impedance. Considering the change of node voltage during the fault, the average value of equivalent impedance is used to study the influence of GMDs on transient stability.

For a GMD intensity (E_x = 0.8 V/km, E_y = 0.4 V/km), substitute the wind farm output power and wind farm access node voltage into (11) and (12), and calculate the

corresponding wind farm output power equivalent grounding impedance, as shown in Fig. 7.

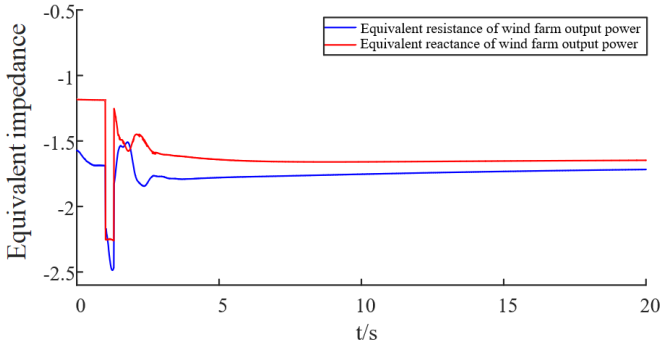

Fig. 7. Equivalent impedance of wind farm output under a certain induced geoelectric field intensity.

When a fault occurs, due to the change of node voltage, the equivalent grounding impedance is variable. For the convenience of calculation, the average value of equivalent impedance between 1s and 1.3s is used to study the impact of GMDs on transient power angle stability.

B. Influence of GMDs on transient stability

For the traditional system, that is, when k_S=0, under the four operating conditions of low load in winter (LW), high load in winter (HW), low load in summer (LS) and high load in summer (HS), the critical clearing angle of the system is 136.78°, 112.74°, 141.25° and 123.01°. According to the statistics of induced geoelectric fields in 29 GMD events in the 23rd solar activity cycle, the variation range of E_x is - 1~1 V/km, and the variation range of E_y is - 0.4~0.4 V/km. Take these induced geoelectric field components as the limit and calculate GIC-Qs of each substation in steps of 0.1V/km. After the GIC-Q is equivalent to the grounding impedance, the influence of GMDs on the critical clearing angle is shown in Fig. 8.

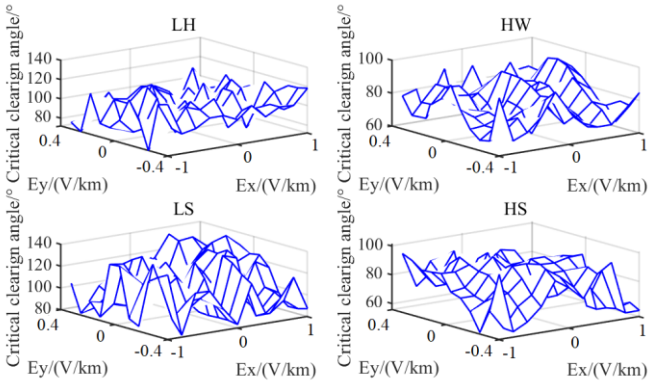

Fig. 8. Change of critical clearing angle

The random of GMDs makes the change of critical clearing angle irregular. But compared with no GMD, the critical clearing angle decrease, so the stability becomes worse.

For the case of $k_S \neq 0$, calculate the critical clearing angle and its partial derivative of k_S. Using the random fuzzy simulation technology and inverse transformation method in Section II-C, set M to 100 to generate induced geoelectric field samples. Then, for each k_S and multiple groups of induced geoelectric field samples, the expected value of the critical clearing angle is calculated by using Section III-C fuzzy simulation, and the variation law of the critical clearing angle with the proportion of wind power is obtained, as shown in Fig. 9.

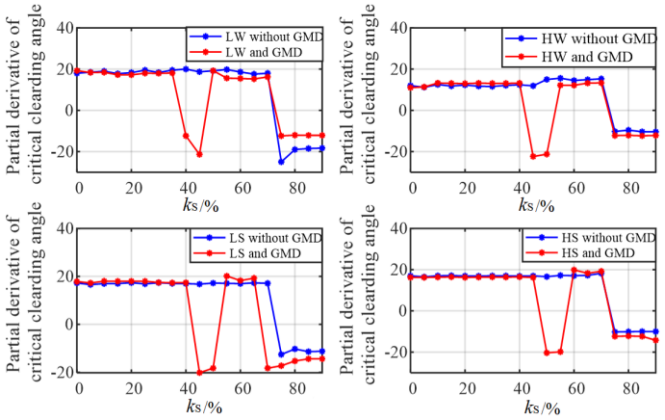

(a)

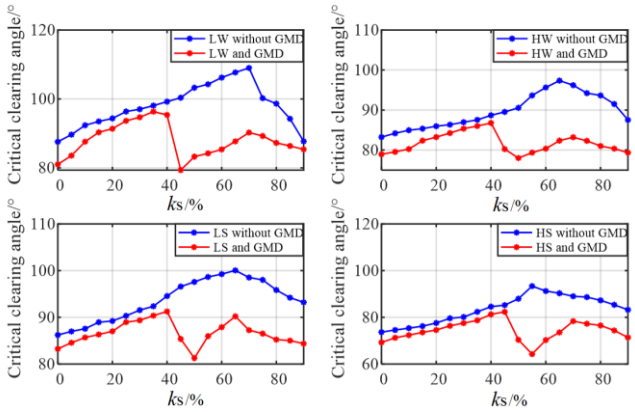

(b)

Fig. 9. Critical clearing angle. (a) Partial derivative of critical clearing angle to k_S. (b) Critical clearing angle of different k_S

For the case without GMDs, the critical clearing angle first rises (k_S is in the range of 0~70%) and then decreases (k_S is greater than 70%). When GMDs occur, the changing trend of critical clearing angles is more complex. The critical clearing angle increases first (k_S is in the range of 0~40%), then decreases (k_S is in the range of 40~50%), then increases (k_S is in the range of 50~70%) and finally decreases (k_S is greater than 70%). The critical clearing angle curve when GMDs occur is below the critical clearing angle curve when GMDs do not occur, so GMDs are not conducive to the system transient stability. And under the HS operation mode, the critical clearing angle of GMD is the smallest.

Under the HS operation mode, the influence of GMDs on acceleration/deceleration area is shown in Fig.10. The power characteristics of normal operation, fault and fault removal are represented by P_{I}, P_{II}, P_{III}, and the black curve is the power characteristics without GMDs. The uncertainty of GMDs makes the electromagnetic power of equivalent

system not a fixed curve, but a cluster of red curves. The blue curves are envelopes of electromagnetic power during normal operation in the case of GMDs. The cyan curves are envelopes of electromagnetic power in case of fault and GMDs. The green curves are envelopes of electromagnetic power after the fault is removed.

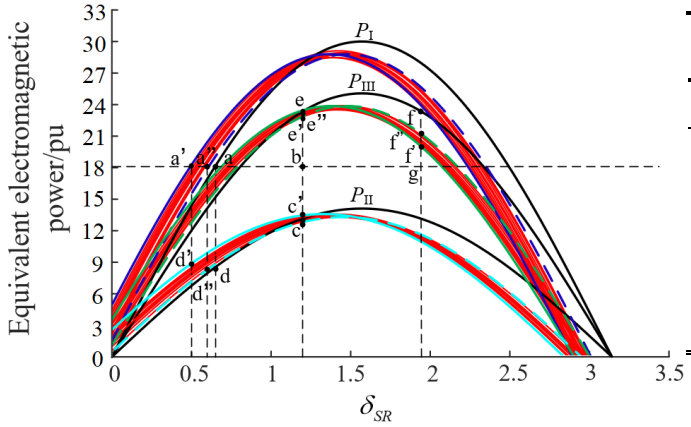

(a)

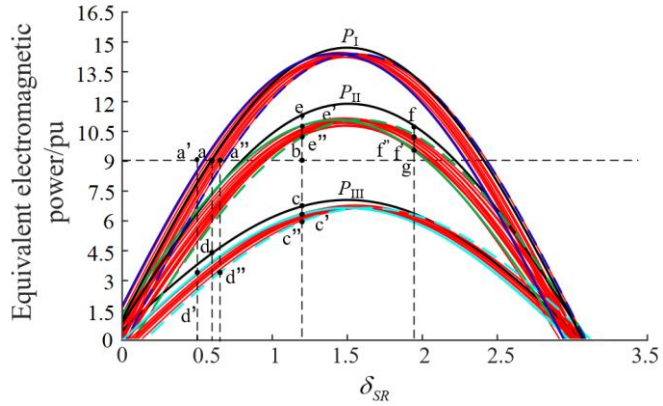

(b)

Fig. 10. Equivalent electromagnetic power characteristics. (a) Electromagnetic power curve at k_S = 0%. (b) Electromagnetic power curve at k_S=50%.

S_{abcd} in Fig.10 is the acceleration area without GMDs, $S_{a'bc'd'}$ and $S_{a'bc'd'}$ are the acceleration area composed of the envelope of equivalent electromagnetic power curve when GMDs occur, and the change of acceleration area cannot be obtained directly. S_{efgb} is the deceleration area without GMDs, and $S_{e'f'gb}$ and $S_{e'f'gb}$ are the deceleration area composed of the envelope of the equivalent electromagnetic power curve when GMD occurs. The deceleration area decreases when GMDs occur in both conventional systems and hybrid systems. The acceleration area S_{ac} and deceleration area S_{dc} in case of GMDs and no GMDs under different wind power access ratios are shown in Table III and Table IV. F represents without GMDs and T represents the occurrence of GMDs.

TABLE III
Expected value of acceleration area under different wind power ratio

k_S/%	LW		HW		LS		HS	
	F	T	F	T	F	T	F	T
0	98.1	106.5	100.2	103.4	99.6	101.2	100.3	102.3
10	91.2	96.2	92.3	99.5	92.3	97.6	95.6	98.6
20	85.2	90.6	86.9	95.6	83.6	95.3	90.3	96.3
30	80.3	86.4	82.3	89.2	80.1	91.5	85.6	93.4
40	76.5	110.2	78.2	82.3	77.8	87.6	80.3	90.2
50	70.4	95.4	73.6	93.2	72.3	100.2	75.6	102.3
60	65.2	84.2	70.2	90.1	67.3	94.5	80.6	96.1
70	60.2	71.3	79.8	92.6	72.3	96.5	83.9	95.3
80	79.8	85.6	86.5	95.8	82.3	97.6	90.2	98.3
90	97.3	100.2	94.9	96.8	78.6	98.1	92.3	99.6

TABLE IV
Expected value of deceleration area under different wind power ratio

k_S/%	LW		HW		LS		HS	
	F	T	F	T	F	T	F	T
0	114.2	112.7	113.6	110.5	110.2	108.1	108.6	107.2
10	120.3	116.9	119.2	113.6	115.6	114.2	113.8	110.3
20	126.8	119.3	121.3	118.4	119.8	118.1	116.5	116.9
30	129.8	123.2	128.6	121.6	124.6	121.6	120.1	118.3
40	136.4	120.3	131.4	128.3	130.1	125.9	126.9	120.9
50	142.5	128.9	136.8	115.3	136.9	110.1	128.9	108.9
60	148.9	134.6	142.1	118.9	143.5	114.2	124.3	110.2
70	151.0	139.5	140.3	115.6	135.2	110.3	120.1	115.3
80	132.1	120.6	125.6	113.2	131.5	108.9	118.4	107.2
90	115.6	110.2	101.6	110.3	136.5	106.3	115.3	102.1

Firstly, the acceleration/deceleration areas in Tables III and IV are compared horizontally. For a certain wind power ratio, when GMDs occur, the acceleration area increases and the deceleration area decreases under any operation mode. Then a longitudinal comparison is made. For the different proportions of wind farm output power, when GMDs do not occur, the acceleration area decreases first (0~70%) and then increases (greater than 70%), and the deceleration area increases first (0~70%) and then decreases (greater than 70%). When GMDs occur, the acceleration decreases first (0~40%), then increases (40~50%), then decreases (50~70%) and finally increase (greater than 70%). The deceleration increases first 0~40%), then decreases (40~50%), then increases (50~70%) and finally decreases (greater than 70%). This indicates that when GMDs occur, the optimal wind power access ratio decreases, and the system's ability to accept wind power decreases. The trend of acceleration/deceleration area can explain the change of critical clearing angle in Fig. 9. The stability margin η is shown in Fig. 11.

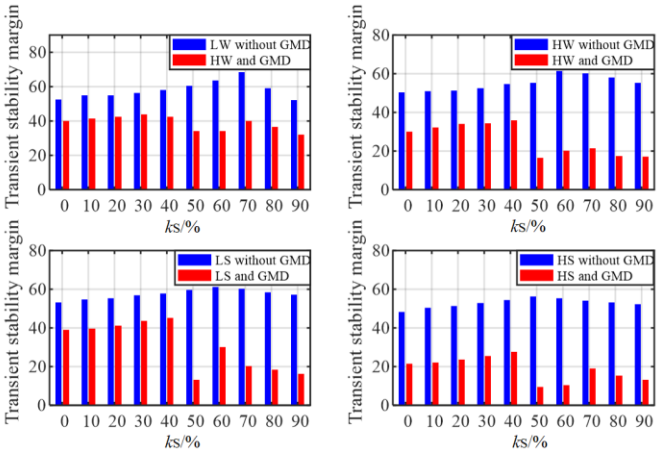

Fig. 11. Transient stability margin.

Without GMDs, under the four operation modes, the transient stability margin increases with the increase of wind power access proportion (0~70%). After exceeding 70%, the

transient stability margin decreases with the increase of wind power access proportion. When GMDs occur, no matter which operation mode, the transient stability margin is lower than that without GMDs. The transient stability margin increases first (about 0~40%), then decreases (40%~50%), then increases (50%~70%), and finally decreases (more than 70%). Under the operation mode of HS and when the proportion of wind farm output power reaches about 50%, the transient stability margin is the lowest.

C. Simulation verification

The equivalent power angle curve is different under the different proportions of wind power output power. Taking the wind power access ratio of 50% as an example, under the HS operation mode, the equivalent power angle curve is shown in Fig. 12. Under the four operating modes, the first swing angle difference under different wind power ratios is shown in Table V, where the data inside and outside the brackets are the power angle difference when GMDs occur and when GMDs do not occur.

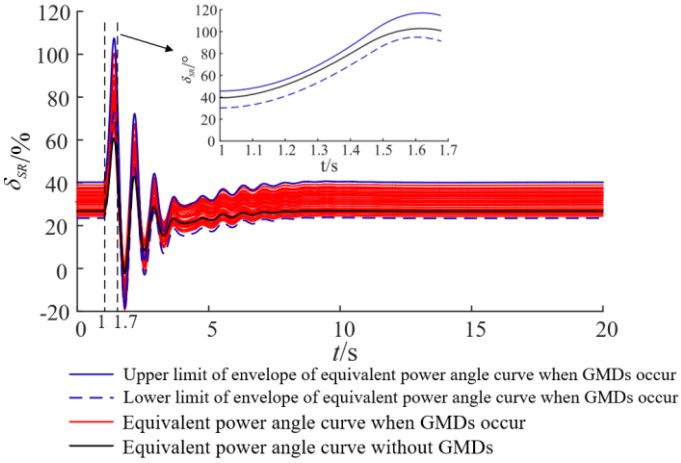

Fig. 12. Equivalent power angle curve

Several red curves (power angle difference) in Fig. 12 are caused by the uncertainty of the IGF when GMDs occur. The random fuzzy simulation is used to generate IGF samples to calculate GIC-Q. Adding different GIC-Q as reactive loads to the system can inevitably produce different power flow calculation results and different initial states, so there will be many different power angle difference curves. When GMDs occur, the acceleration area increases, the deceleration area increases, and the expected value of transient stability margin decreases. According to the EEAC, the transient stability is reduced, which is shown in the time-domain simulation curve of power angle difference, that is, the amplitude increases and the oscillation time prolongs. The results of Fig. 10 and Table IIII are verified.

TABLE V
Power angle difference of first swing under different wind power ratio

k_S/%	Operation mode			
	LW	HW	LS	HS
0	90.2(105.6)	100.7(120.8)	98.5(110.4)	106.9(132.5)
10	83.2(95.6)	97.6(110.5)	90.5(100.3)	103.4(123.5)
20	74.8(87.6)	86.9(98.6)	86.2(96.2)	99.1(115.6)
30	70.4(83.6)	80.2(94.6)	80.4(84.6)	98.6(110.5)
40	61.3(74.6)	74.6(80.3)	74.2(78.6)	97.3(98.5)
50	50.3(103.5)	65.3(100.6)	69.5(100.7)	96.3(118.6)
60	42.8(95.6)	62.0(92.3)	62.1(86.3)	84.3(112.3)
70	71.2(84.6)	87.6(80.7)	61.7(84.3)	90.4(105.6)
80	85.5(89.6)	95.6(98.3)	74.5(92.1)	92.5(110.4)
90	100.6(96.2)	105.9(108.4)	89.5(100.4)	96.8(121.3)

First, make a longitudinal comparison, that is, compare the power angle difference of different wind power proportions under the same operation model. The wind power integration makes the power angle difference decrease. With the increase of the wind power ratio, the power angle of the first swing decreases. When GMDs do not occur, for LW, HW, LS and HS operation modes, when the wind power ratio reaches 60%, 60%, 70% and 60% respectively, the descent process stops. When GMDs occur, for LW, HW, LS and HS operating modes, the descent process stops when the wind power ratio reaches 40%, 50%, 40% and 40% respectively. Therefore, when GMD occurs, the optimal wind power access ratio decreases. Then make a horizontal comparison, that is, compare the power angle difference of different operation modes under the same wind power ratio. When the GMDs occur, no matter which operation mode, the first swing angle is greater than that when GMDs do not occur, and the first swing angle is the largest under the HS operation mode. In the case of GMDs, the variation of critical clearing angle, first swing angle difference and transient stability margin with the proportion of wind power access are consistent, which verifies the correctness of the conclusion.

V. CONCLUSION

In this paper, through the correlation between the induced geoelectric field, GIC-Q and the equivalent rotor motion equation, it was proved that GMDs could affect not only the voltage stability, but also the transient power angle stability of the system. By quantitatively evaluating the impact of GMDs on transient stability based on the Mengdong power grid, conclusions are given as follows:

1) Based on the 29 strong GMDs in the 23rd solar activity cycle, the induced geoelectric fields were calculated, and the probability distribution analysis and fuzzy feature extraction of distribution parameters were carried out. The results showed that the induced geoelectric field components obey t location-scale distribution, and its shape parameters, scale parameters and location parameters are fuzzy, but its boundary can be defined within a certain confidence interval to obtain its membership function. Therefore, the induced geoelectric fields can be regarded as a random fuzzy variable to study the influence of GMDs on the stability of the power system.

2) The GMDs, an uncertain factor, could affect the expected value of critical clearing angle, the expected value of acceleration/deceleration area and transient stability margin. Compared to the case without GMDs, when GMDs occur, the critical clearing angle and transient margin of the system were reduced in any operation mode. Under the operation mode of heavy load in summer, when the proportion of wind farm output power reached about 50%, the transient stability margin of the system was the smallest. Therefore, GMDs could deteriorate the transient stability of

the system.

REFERENCES

[1] T. J. Overbye, T. R. Hutchins, K. Shetye, et al, "Integration of geomagnetic disturbance modeling into the power flow: A methodology for large-scale system studies," in *2012 North American Power Symposium (NAPS)*, Champaign, IL, USA, 2012, pp. 1-7.

[2] G. P. Juvekar, C. Klauber, K. R. Davis, et al, "GIC-Inclusive State Estimator for Power System Awareness During Geomagnetic Disturbance Events," *IEEE Trans. Power Syst.*, vol. 36, no. 4, pp. 2966-2974, Jul. 2021.

[3] T. J. Overbye, K. S. Shetye, T. R. Hutchins, Q. Qiu and J. D. Weber, "Power Grid Sensitivity Analysis of Geomagnetically Induced Currents," *IEEE Trans. Power Syst.*, vol. 28, no. 4, pp. 4821-4828, Nov. 2013.

[4] L. Bolduc, "GIC observations and studies in the hydro-quebec power system," Journal of Atmospheric and Solar-Terrestrial Physics, vol. 64, no. 16, pp. 1793-1802, 2002.

[5] LESHER R L, PORTER J W, BYERLY R T, "SUNBURST-a network of GIC monitoring systems," *IEEE Trans. Power Deliv.*, vol. 9, no. 1, pp. 128-137, 1994.

[6] N. A. E. R. Corporation and the United States Department of Energy, "High-impact, low-frequency event risk to the north American bulk power system," 2010.

[7] NERC. 2012 Special reliability assessment interim report-effects of geomagnetic disturbances on the bulk power system[R/OL]. North American Electric Reliability Corporation, 2012[2012-02-29]. http://www.nerc.com/ pa/RAPA/ra/Pages/default.aspx.

[8] Koen J, Gaunt T, "Geomagnetically induced currents in the southern African electricity transmission network," in *Peoceeding of IEEE Bologna Technology Conference*, Bologna, Italy, 2003, pp. 1-7

[9] Beland J, Small K, "Space weather effects on power transmission systems: the cases of hydro-quebec and transpower New ZealandLTD," *Springer Netherlands*, vol. 176, pp. 2550-5, 2005.

[10] Marshall R A, Smith E A, Francis M J, *et al*., "A preliminary risk assessment of the Australian region power network to space weather," *Space Weather*, vol. 9, no. 10, Oct. pp. 1-18, 2011.

[11] Li Haiming, Tao Yong, Zhang Junshuang, et al. "Risk assessment of Mengdong Power Grid Accident Based on Geomagnetic Storm in March 1989," Power System Technology, vol. 44, no. 11, pp. 4427-4434, Dec. 2020.

[12] A. Haddadi, R. Hassani, J. Mahseredjian, L. Gérin-Lajoie and A. Rezaei-Zare, "Evaluation of Simulation Methods for Analysis of Geomagnetic Disturbance System Impacts," *IEEE Trans. Power Deliv.*, vol. 36, no. 3, pp. 1509-1516, Jun. 2021.

[13] Liu Chunming, Wang Hongmei, Wang Xuan, "Statistical Analysis of Geomagnetically Induced Currents in UHV Power Grids Under Multiple Geomagnetic Storms," *Proceedings of the CSEE*, vol. 39, no. 15, pp. 4606-4614, Aug. 2019.

[14] A. H. Etemadi and A. Rezaei-Zare, "Optimal Placement of GIC Blocking Devices for Geomagnetic Disturbance Mitigation," *IEEE Trans. on Power Syst.*, vol. 29, no. 6, pp. 2753-2762, Nov. 2014.

[15] Marshall R A, Smith E A, Francis M J, et al, "A Preliminary risk assessment of the Australian region power network to space weather," *Space Weather*, vol. 9, no. 10, pp. 1-18, Oct. 2011.

[16] Wu Weili, Liu Lianguang, Wang Kairang, "Risk Assessment Methods and Models of Power System Fault Due to Geomagnetic Disturbance," *Proceedings of the CSEE*, vol. 35, no. 4, pp. 830-839, Feb. 2015.

[17] H. Zhu and T. J. Overbye, "Blocking device placement for mitigating the effects of geomagnetically induced currents," *IEEE Trans. on Power Syst.*, vol. 30, no. 4, pp. 2081-2089, Jul. 2014.

[18] [Online]. Available: http://www.geomag.org.cn/WebRelation.aspx. Accessed on: Feb, 2015.

[19] R. Horton, D. Boteler, T. J. Overbye, R. Pirjola and R. C. Dugan, "A Test Case for the Calculation of Geomagnetically Induced Currents," *IEEE Trans. Power Deliv*, vol. 27, no. 4, pp. 2368-2373, Oct. 2012.

[20] V. D. Albertson, J. G. Kappenman, N. Mohan, et al, "Load-flow studies in the presence of geomagnetically-induced currents," *IEEE Trans. Power APP Syst.*, vol. PAS-100, no. 2, pp. 594-607, Feb. 1981.

[21] Baoding Liu and Yian-Kui Liu, "Expected value of fuzzy variable and fuzzy expected value models," *IEEE Trans. Fuzzy Syst*., vol. 10, no. 4, pp. 445-450, Aug. 2002.

[22] Y. Liu, Y. Miao, A. A. Pantelous, J. Zhou and P. Ji, "On fuzzy simulations for expected values of functions of fuzzy numbers and Intervals," *IEEE Trans. Fuzzy syst*, vol. 29, no. 6, pp. 1446-1459, June 2021

[23] Rui Ma, Qiang Zhang, Xia Wu, et al, "Random Fuzzy Uncertain Model for Daily Wind Speed," *Proceeding of the CSEE*, vol. 35, no. 24, pp. 6351-6358, Dec. 2002.

[24] R. A. Walling and A. N. Khan, "Characteristics of transformer exciting-current during geomagnetic disturbances," *IEEE Trans. Power Del.*, vol. 6, no. 4, pp. 1707-1714, Oct. 1991.

[25] K. S. Shetye, T. J. Overbye, Q. Qiu, et al, "Geomagnetic disturbance modeling results for aep system: A case study," in Proc. *IEEE Power Energy Soc. Gen. Meeting*, Jul. 2013, pp. 1-5.

[26] Y. Si, Z. Wang, L. Liu and A. Anvari-Moghaddam, "The Influence of Geomagnetic Disturbance on Transient Power Angle Stability of Hybrid Systems," *2022 IEEE International Conference on Environment and Electrical Engineering and 2022 IEEE Industrial and Commercial Power Systems Europe (EEEIC / I&CPS Europe)*, 2022, pp. 1-6.

[27] Jiang Huilan, Zhou Zhaoqing, Cai Jichao, "Analysis method of Influence of Wind Power Access Proportion on Transient Power Angle Stability of Power System," Electric Power Automation Equipment, vol. 40, no. 7, pp. 53-61, July 2020.

Yuan SI was born in Hebei, China. He received the B.S. degree in automation specialty from the Institute of Technology of Changchun, in 2017. He is currently pursuing the Ph.D. degree in electrical engineering with North China Electric Power University, Beijing, China.

Since 2019, he has been with Beijing Key Laboratory of High Voltage and Electromagnetic Compatibility, North China Electric Power University. His research interests include safe operation of power grid and catastrophe control, HVDC grounding electrode modeling and impact assessment.

ZEZHONG WANG was born in Shandong, China, in 1960. He received the B.Eng., M.Eng., and Ph.D. degrees in electrical engineering from Tsinghua University, in 1983, 1986, and 1989, respectively. He is currently a Professor and a Doctoral Supervisor with the School of Electrical and Electronic Engineering, North China Electric Power University. His research interests include electromagnetic field numerical analysis, electromagnetic compatibility, and electromagnetic measurement.

LIANGUANG LIU was born in Jilin Province, China, in 1954. He received the M.Sc. degree in electrical engineering from North China Electric Power University, Beijing, China, in 1994. He has been a Professor and a Doctoral Supervisor at the School of Electrical and Electronic Engineering of North China Electric Power University. He is one of experts entitled to the Government Special Allowance (GSA) of China. Mr. Liu is a Senior Member of the Chinese Society for Electrical Engineering

and Commissioner of the Chinese Space Weather Committee and National Space Weather Monitoring and Pre-Warning Technology Standard Committee.

Amjad Anvari-Moghaddam (S'10 - M'14 -SM'17) received the Ph.D. degree (Hons.) in Power Systems Engineering in 2015 from University of Tehran, Tehran, Iran. Currently, he is an Associate Professor and Leader of Intelligent Energy Systems and Flexible Markets (iGRIDS) Research Group at the Department of Energy (AAU Energy), Aalborg University where he is also acting as the Vice-Leader of Power Electronic Control, Reliability and System Optimization (PESYS) and the coordinator of Integrated Energy Systems Laboratory (IES-Lab). His research interests include planning, control and operation management of microgrids, renewable/hybrid power systems and integrated energy systems with appropriate market mechanisms. He has (co)authored more than 280 technical articles, 7 books and 17 book chapters in the field. Dr. Anvari-Moghaddam serves as the Associate Editor of several leading journals such as the IEEE TRANSACTIONS ON POWER SYSTEMS, IEEE Systems Journal, IEEE Open Access Journal of Power and Energy, and IEEE Power Engineering Letters. He is the Vice-Chair of IEEE Denmark and IEEE-PES Danish Chapter and serves as a Technical Committee Member of several IEEE PES/IES/PELS and CIGRE working groups. He was the recipient of 2020 DUO - India Fellowship Award, DANIDA Research Fellowship grant from the Ministry of Foreign Affairs of Denmark in 2018 and 2021, IEEE-CS Outstanding Leadership Award 2018 (Halifax, Nova Scotia, Canada), and the 2017 IEEE-CS Outstanding Service Award (Exeter-UK).